



LAWRENCE
LIVERMORE
NATIONAL
LABORATORY

HF-based etching processes for improving laser damage resistance of fused silica optical surfaces

T.I. Suratwala, P.E. Miller, J.D. Bude, R.A. Steele, N. Shen, M.V. Monticelli, M.D. Feit, T.A. Laurence, M.A. Norton, C.W. Carr, L.L. Wong

March 5, 2010

Journal of the American Ceramic Society

Disclaimer

This document was prepared as an account of work sponsored by an agency of the United States government. Neither the United States government nor Lawrence Livermore National Security, LLC, nor any of their employees makes any warranty, expressed or implied, or assumes any legal liability or responsibility for the accuracy, completeness, or usefulness of any information, apparatus, product, or process disclosed, or represents that its use would not infringe privately owned rights. Reference herein to any specific commercial product, process, or service by trade name, trademark, manufacturer, or otherwise does not necessarily constitute or imply its endorsement, recommendation, or favoring by the United States government or Lawrence Livermore National Security, LLC. The views and opinions of authors expressed herein do not necessarily state or reflect those of the United States government or Lawrence Livermore National Security, LLC, and shall not be used for advertising or product endorsement purposes.

HF-based etching processes for improving laser damage resistance of fused silica optical surfaces

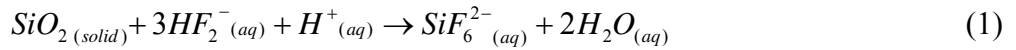
T. I. Suratwala, P. E. Miller, J. D. Bude, R. A. Steele, N. Shen, M. V. Monticelli, M. D. Feit,
T. A. Laurence, M. A. Norton, C. W. Carr, L. L. Wong
Lawrence Livermore National Laboratory, P.O. Box 808, Livermore, CA 94551, USA

The effect of various HF-based etching processes on the laser damage resistance of scratched fused silica surfaces has been investigated. Conventionally polished and subsequently scratched fused silica plates were treated by submerging in various HF-based etchants (HF or $\text{NH}_4\text{F}:\text{HF}$ at various ratios and concentrations) under different process conditions (e.g., agitation frequencies, etch times, rinse conditions, and environmental cleanliness). Subsequently, the laser damage resistance (at 351 or 355 nm) of the treated surface was measured. The laser damage resistance was found to be strongly process dependent and scaled inversely with scratch width. The etching process was optimized to remove or prevent the presence of identified precursors (chemical impurities, fracture surfaces, and silica-based redeposit) known to lead to laser damage initiation. The redeposit precursor was reduced (and hence the damage threshold was increased) by: 1) increasing the SiF_6^{2-} solubility through reduction in the NH_4F concentration and impurity cation impurities, and 2) improving the mass transport of reaction product (SiF_6^{2-}) (using high frequency ultrasonic agitation and excessive spray rinsing) away from the etched surface. A 2D finite element crack-etching and rinsing mass transport model (incorporating diffusion and advection) was used to predict reaction product concentration. The predictions are consistent with the experimentally observed process trends. The laser damage thresholds also increased with etched amount (up to $\sim 30\text{ }\mu\text{m}$), which has been attributed to: 1) etching through lateral cracks where there is poor acid penetration, and 2) increasing the crack opening resulting in increased mass transport rates. With the optimized etch process, laser damage resistance increased dramatically; the average threshold fluence for damage initiation for $30\text{ }\mu\text{m}$ wide scratches increased from 7 to 41 J/cm^2 , and the statistical probability of damage initiation at 12 J/cm^2 of an ensemble of scratches decreased from $\sim 100\text{ mm}^{-1}$ of scratch length to $\sim 0.001\text{ mm}^{-1}$.

1. INTRODUCTION

Improved laser damage resistance of fused silica optical surfaces has been a quest for several decades for use in high-peak-power laser systems such as the National Ignition Facility. In the past decade, laser damage initiation density has been reduced significantly using improved finishing processes [1-4] and post-fabrication laser mitigation techniques [5] (see Fig. 1). Depending on the finishing or post processing, the fused silica optics typically exhibit laser damage when exposed to 351nm, 3 ns laser pulses at fluences from 5-15 J/cm², whereas the intrinsic surface damage threshold is >100 J/cm². Hence there is still much room for improvement. Wet chemical etching is another attractive post processing treatment, having the advantages of: 1) potentially removing and mitigating the identified absorbing precursors leading to laser damage initiation; 2) globally treating the whole fused silica optic simultaneously; and 3) ultimately leading to less reliance on very challenging scratch/dig specifications on the finishing processes.

Aqueous fluoride-based etching (e.g., HF and NH₄F:HF) has historically been used to etch silica glass for a variety of applications including: 1) glass cleaning; 2) removal of native oxides during Si wafer processing; 3) etching gratings and other structures on glass [6]; and 4) blunting surface cracks to increase the mechanical strength of glass. In recent work [2,7], etching has also been used to: 1) expose hidden surface fractures as a diagnostic for the presence of sub-surface damage, and 2) reduce the amount of polishing required after grinding. Aqueous fluoride-based etching typically isotropically removes silica from the surface with the overall reaction:



The aqueous phase reaction product SiF₆²⁻ will have limited solubility in the solution, which will depend on the cation concentration present in the etchant solution [8].

The use of etching to improve laser damage has had some success; however, a lack of detailed understanding of both the etching process and the precursors that lead to laser damage initiation have prevented the predictability and reproducibility of the results. In 1997, Yoshiyama et. al. [9] showed that removal of up to 200 nm from the silica surface resulted in an increase in the damage threshold. Battersby et. al. (1998) [10] observed a similar trend with the reduction in the ‘gray haze’-type damage and an increase in the damage threshold. These improvements are likely due to the removal of the impurities in the polishing or Beilby layer. Further etching often resulted in a decrease rather than an increase in the damage threshold. This group hypothesized it was possibly due to uncovering further contaminants, uncovering more sub-surface damage, and/or redeposit of the contaminants. Others have later shown that HF etching can be an effective method to mitigate pre-existing damage sites. However, statistical confidence on the percentage of sites mitigated was limited [11-13].

In these studies, the chemical etching techniques for improving laser damage resistance were focused on removing impurities from the silica surface and the ‘removal’ of sub-surface damage. However, it was not yet clear what were the nature and characteristics of the precursors that lead to laser damage initiation. In a recent study [14], these precursors (see Fig. 2) were systematically isolated and identified as: 1) impurities (e.g., Ce, Fe, etc.) in the 50-100 nm Beilby layer; 2) a shallow intrinsic defect layer found on fracture surfaces (such as scratches); and 3) redeposited silica compounds comprising of intrinsic/extrinsic absorbing defects. All three of these precursors lead to a localized optical absorption below the band gap of bulk silica glass ultimately leading to laser damage when exposed to laser fluence [15].

With the identification of these precursors, one can now systematically identify and optimize treatments to optical surfaces to remove or mitigate these precursors. In our previous study [14], etching has been shown to be effective at both removing the impurities in the Beilby layer as well as removing the intrinsic defect layer on isolated cracks. The latter precursor, redeposited silica compounds, has been found to be more challenging to prevent.

In the following study, a systematic investigation of aqueous fluoride-based etch processing has been conducted largely focused on strategies to preventing the redeposit. These optimized etch processes have significantly improved the surface damage threshold of fused silica (see Fig. 1). More specifically, the etching process improvement has been largely driven by: 1) increasing the solubility of the reaction product by reducing the cation concentration to prevent redeposit; 2) improving the mass transport of the reaction product (SiF_6^{2-}) during the etching and rinsing to prevent redeposit; and 3) etching the appropriate amount to remove the Beilby layer and fracture surface layer, to etch through the lateral cracks, and to achieve crack morphologies to maximize mass transport rates. These patented, optimized etching processes [16] are now being used to improve the laser damage resistance of critical fused silica optics used in high-peak-power lasers such as the National Ignition Facility.

2. EXPERIMENTAL

2.1 Fused Silica Sample Preparation

Fused silica plates (50 mm in diameter x 10 mm thick; Corning 7980 or Heraeus Suprasil 314) were ground and polished using conventional ceria polishing techniques (Sydor Optics). The samples were then scratched by single pass, unidirectional sliding (~ 0.6 psi; velocity ~ 0.5 m/s) of one face on a dry polyurethane polishing pad (Suba 550) sprinkled with approximately a hundred 200 μm diameter silica spheres. This resulted in set of unidirectional scratches typically 10-35 μm in width with ~ 100 μm spacing between scratches. The total scratch length on a typical sample was ~ 2.5 m which allowed for statistical evaluation of the laser damage initiation of the scratches. Note the scratch morphology in these samples was typical of the scratches observed during polishing. The scratch morphology is characterized as brittle, trailing indent scratches often containing lateral cracks (see [17] for description of various scratch morphology types).

2.2 Etching Process

The scratched samples were then treated by submerging them in various HF-based etchants (HF (2.5-49%) or $\text{NH}_4\text{F}:\text{HF}$ at various ratios and concentrations) under different agitation conditions (static, ultrasonic or megasonic conditions at various frequencies), etch times, as well as post-etch aqueous rinsing conditions. A description of the detailed process parameters used for each of the samples is shown in Table 1. The sample was first submerged in a polypropylene tank filled with the acid and agitation was generated using a Teflon-lined, multi-frequency ultrasonic transducer (Blackstone multiSONIK™ 40, 80, 120, 140, 170, 220 and 270 kHz and multMEG™ 430, 1300 kHz). Subsequently the sample was removed and submerged in a de-ionized water rinse tank also agitated with a similar ultrasonic transducer. Finally, the sample was water spray rinsed using de-ionized water and allowed to air dry. During the etching and rinsing processes, samples were mounted in Teflon frames held only on the edges of the sample.

2.3 Laser Damage Testing

The samples were then tested by small beam (80 μm) and/or by large beam (3 cm) laser damage testing while the scratches were oriented on the exit surface of the incident laser light. The small beam testing allowed for testing the laser damage threshold of a single crack at a time by ramping up the fluence until damage was observed [18]. A Q-switched Nd:YAG laser (Coherent Infinity) was used to provide 355 nm laser light (3ns pulse, temporal and spatial profile Gaussian, beam waist $1/e^2$ diameter 80 μm). The average and the standard deviation of the threshold fluence at damage (as determined by in-situ optical microscopy) were recorded after laser initiating between 10-60 scratch locations per sample.

The large beam testing, on the other hand, tested a large number of scratches simultaneously at a fixed fluence. The testing was conducted on selected samples using the Optical Sciences Laser (OSL) (see [19] for description of laser system). The samples were shot at 351 nm (5 ns flat in time, 3 cm beam diameter) at a target fluence of 8, 10 or 12 J/cm^2 . Pre-shot and post-shot images (VIEW microscope scans at 5x magnification) of the entire laser exposed area were differenced to obtain the number of initiated sites per unit length of scratch. The laser beam fluence is recorded with a 16 bit scientific grade CCD camera and is spatially registered to the VIEW microscope image montage to obtain the damaging fluence (see [20] for a general description of the techniques employed). Note that the small beam testing allows for determining the average damage threshold for a given scratch, while the large beam testing provides a statistical likelihood of obtaining damage at a given fluence for a given length of scratch. Hence, the large beam testing results can be used to predict expected number of damage sites over large number of scratches or large areas of an optical surface (e.g., optics used in high peak power laser systems).

3. RESULTS

Table 1 summarizes the various processes used and the small beam laser initiation fluence for scratches with widths between 20-30 μm . The laser damage resistance of scratches on the silica surface was found to be very etch process dependent. The small beam laser damage resistance of these scratches ranged from $\sim 5\text{-}7 \text{ J}/\text{cm}^2$ (for the untreated or statically etched scratches) to $>40 \text{ J}/\text{cm}^2$ (using the optimized etch process). The laser damage resistance was also strongly scratch

width (w) dependent, where damage fluence scaled roughly as $1/w$. This is illustrated in Fig. 3 where the small beam laser initiation fluence is plotted as a function of various pre-etch, scratch widths for various etching processes. Note each point on the plot represents a single set of neighboring trailing indent cracks along the scratch and its corresponding scratch width and initiation fluence. On the same figure, it is convenient to illustrate the effect of the major process variables on the laser damage resistance of the scratches. With increase in agitation (using high frequency ultrasonics) during etching and rinsing, with change in fluoride acid composition, and with improvements in cleanliness, there is a significant increase in the threshold fluence for laser damage that still scales with scratch width. Figure 4 shows both the small beam and large beam laser damage results as a function of etched amount for the various major process variations. Using the optimized acid etch process (with sample series H and G), one finds that 20-30 μm of material needs to be etched to maximize the laser damage resistance of the scratch.

Figure 5 shows optical micrographs of scratches from three selected samples illustrating both the change in morphology of the scratches and the resistance to laser damage after large beam testing. After etching the scratches become more visible (compare Fig. 5 b and c with Fig. 5a). After exposing these surfaces to high fluence (12 J/cm^2), there is a dramatic decrease in the number of sites initiated, especially with Sample G4 (Fig. 5f) where essentially no sites were initiated.

Figure 6 shows optical micrographs (left side) and the corresponding fast photoluminescence [15] (right side) images of a scratch processed using a static etch and rinse (top) (Sample B2) compared with using ultrasonic etch and rinse (bottom) (Sample F3). In a previous study [15], it has been shown that the presence of fast photoluminescence lifetimes ($<1 \text{ ns}$) is an indication of absorption that is linked to laser damage at 351nm. Both the optical micrographs and photoluminescence illustrate the presence of foreign matter in the cracks after the static etch with Sample B2. With the addition of agitation, the foreign matter is dramatically reduced, also leading to reduced photoluminescence and increased laser damage threshold. Another example is shown in Fig. 7a, which shows a scanning electron micrograph of a scratch on Sample F8, illustrating the presence of foreign material and its preferential redeposit on the edge of the etched cusps. In addition, when the etched scratches damage at high fluence, it almost always initiates at the edge of the cusps (for example, see Figs. 7b and c). Figure 8 shows an x-ray diffraction pattern of crystallites formed after intentionally etching silica glass for very long times in a relatively small etch solution volume. The formation of an ammonium hexafluorosilicate compound is identified, which is the likely candidate for the material redepositing in the cracks.

4. DISCUSSION

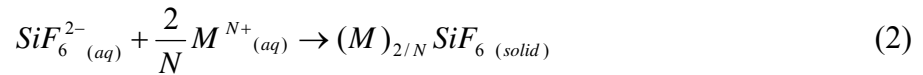
As discussed above, aqueous fluoride-based etching is an attractive method to remove or prevent the three identified surface precursors (Fig. 2). A key challenge of this type of etch process is to prevent the redeposition (see Figs. 6 and 7) of the reaction products by transporting them away from the surface before they precipitate or redeposit. In the following discussion, two methods are described to reduce the precipitation products: 1) control the chemistry to increase reaction product solubility (Section 4.1); and 2) increase the mass transport of reaction products away from the surface through agitation and spray rinsing (Section 4.2). Finally, an explanations are

given as to why laser damage performance increases with the etch amount up to 20-30 μm (Section 4.3).

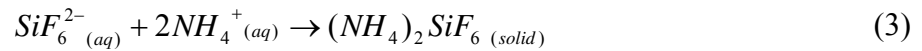
4.1 Reaction Product Solubility

Wet chemical etching of silica can be accomplished using a variety of reagents including aqueous HF and $\text{NH}_4\text{F}:\text{HF}$. The latter, commonly referred to as buffered-oxide-etch (BOE), is routinely used in the electronics industry because it results in more stable etch rates and because of its comparatively lower vapor pressures. In the following study, both sets of etchants (HF and BOE) were used in various concentrations and/or various ratios (see Table 1). For both sets of acids, the overall reaction for the dissolution of silica glass is described by Eq. 1, where the bifluoride anion (HF_2^-) is formed in solution as the active species to react with silica surface to form the stable reaction product (SiF_6^{2-}) dissolved in solution [7,8].

From the results described above, there is an association between the deposit found in the etched cracks and its laser damage threshold. This material has been identified as a hexafluorosilicate compound that precipitates in the crack during the etch, rinse or drying stages of the process. The formation of a hexafluorosilicate precipitate can be written in the general form:



where M is the cation species and N is the charge state of the cation. For example, using BOE, where the cation is ammonium (NH_4^+), the reaction is given by:



where the reaction product is ammonium hexafluorosilicate $(\text{NH}_4)_2\text{SiF}_6$. The equilibrium constant for Eq. 3 is given by:

$$K_{sp} = [\text{NH}_4^+]^2 [\text{SiF}_6^{2-}] = 1.94 \left(\frac{\text{mol}}{\text{liter}} \right)^3 \quad (4)$$

The solubility of SiF_6^{2-} can be increased by reducing the NH_4^+ concentration. Because NH_4F in solution is expected to completely dissociate (i.e., $[\text{NH}_4\text{F}] \cong [\text{NH}_4^+]$), the hexafluorosilicate solubility can be described as:

$$S_{\text{SiF}_6^{2-}} = \frac{1.94 \left(\frac{\text{mol}}{\text{liter}} \right)^3}{[\text{NH}_4\text{F}]^2} \quad (5)$$

where the solubility scales inversely as the square of ammonium fluoride concentration of the BOE.

Commercially available BOE (NH₄F:HF) is typically described by the volume ratio of the 40 wt% NH₄F to 49 wt% HF. Figure 9a shows the estimated solubility for SiF₆²⁻ using Eq. 5 as a function of BOE ratio scaled to match the etch rate of 20:1 BOE (1.74 μm/hr) by diluting or concentrating the acid. The solubility increases from 18 mol/m³ for 20:1 BOE to 215 mol/m³ for 6:1 BOE (diluted 3x). We believe this change in solubility, by changing the acid from 20:1 BOE to 6:1 BOE (diluted 3x) (as can be seen in Table 1 and Figs. 3 and 4), is a key factor leading to the improvement in damage threshold. A further way to increase the SiF₆²⁻ solubility is to eliminate the presence of the ammonium cation all together, such as using only an HF acid system as conducted with Samples H1-H13. The results from the HF etch compositions (H series samples) were equivalent to the 6:1 BOE (diluted 3x) composition performed in a class 100 cleanroom (G series samples) (again see Table 1 and Figs. 3 and 4).

Other cations, in addition to NH₄⁺, can also precipitate the hexafluorosilicate anion (Eq. 2). The solubility of both SiF₆²⁻ and H₂F₂¹⁻ anions with various cations is shown in Fig. 9b. Common cations, such as K¹⁺ and Na¹⁺, form hexafluorosilicate salts which have a significantly lower solubility than NH₄⁺, and hence stress the importance of minimizing the presence of these impurities during the etching and rinsing process. To test this, Sample E1 was etched while doped with 500 ppm by weight Na; this sample had a noticeably lower laser damage threshold than its undoped counterpart (sample E2). For the G series samples, contamination was further minimized using electronic grade acids, performing the etch process in a class 100 cleanroom, and using higher purity deionized water (resistivity >18 MΩ). The G Series samples performed noticeably better than their counterpart (F series) particularly for large amounts of silica removed during etching. This improvement has been largely attributed to the lower concentrations of impurity cations.

4.2 Mass Transport

4.2.1 2D Mass Transport Model

In addition to increasing the solubility of the reaction products, improving the mass transport of the reaction products away from the surface was also used to minimize hexafluorosilicate redeposit or precipitation. A significant improvement in laser damage threshold was observed for samples treated by high frequency ultrasonics during etching and rinsing (see Fig. 3). Here a 2D mass transport model is described which incorporates the diffusive mass transport of the reaction products away from a boundary layer during etching and rinsing as well as the change in the crack morphology with etched amount. This model provides significant insights to important process variables (e.g., frequency of agitation, etch or rinse time, and etched amount) that lead to increase transport of reaction products away from the surface during the etch process.

Consider a parabolic-shaped, single crack on the silica surface having an initial depth d_o and width w_o as shown in Fig. 10. The isotropically etched silica surface will be represented as a moving surface boundary. The shape of the parabolic crack will change as [21]:

$$\frac{dr}{dt} = \frac{r_e}{6} \left(\left(4 + \left(\frac{r}{d_o} \right)^2 \right)^{3/2} - \left(\frac{r}{d_o} \right)^3 - 6 \left(\frac{r}{d_o} \right) \right) \quad (6)$$

where r is the radius of the crack, r_e is the etch rate in $\mu\text{m/hr}$, and t is the etch time. A boundary layer of thickness δ exists between the bulk solution and the silica surface (as designated by a dashed line in Fig. 10). Transport through this layer is assumed to be governed by diffusion (i.e., no convection or chemical affinity of reaction products occurs in the boundary layer) and hence the reaction product (SiF_6^{2-}) concentration (C) is described by Fick's Second Law in 2D as:

$$\frac{\partial C(x, y, t)}{\partial t} = D \nabla^2 C(x, y, t) \quad (7)$$

where D is the concentration-independent diffusion coefficient for SiF_6^{2-} in acid during etching or water during rinsing. During etching the moving silica surface establishes a fixed surface concentration C_s which is simply:

$$C_s = \frac{\rho_{\text{SiO}_2}}{MW_{\text{SiO}_2}} \quad (8)$$

where ρ_{SiO_2} and MW_{SiO_2} are the mass density and molecular weight of silica. Also, the silica surface has the following boundary conditions during the etch and rinse:

$$\begin{aligned} C(\text{surface}, t) &= C_s & (\text{etch}) \\ \frac{dC(\text{surface}, t)}{d\vec{n}} &= 0 & (\text{rinse}) \end{aligned} \quad (9)$$

where \vec{n} is the direction normal to the local surface. The transport out of the boundary layer at $y=\delta$ is described as:

$$\frac{\partial C(x, \delta, t)}{\partial y} = \frac{k_c(t)(C(x, \delta, t) - C_\infty)}{D} \quad (10)$$

where C_∞ is the concentration of the reaction product far away from the surface. $k_c(t)$ is the mass transfer coefficient for a crevice on a surface which is defined as [22]:

$$k_c(t) = 0.332 \frac{D}{w(t)} R_e(t)^{1/2} S_c^{1/3} \quad (11)$$

where $w(t)$ is the scratch width as a function of etch time, $R_e(t)$ is the Reynolds number as a function of etch time, and S_c is the Schmidt number which are all defined respectively as [22]:

$$w(t) = 2 r(t) \quad (12)$$

$$R_e(t) = v \frac{\rho}{\mu} w(t) \quad (13)$$

$$S_c = \frac{\mu}{\rho D} \quad (14)$$

where v is the fluid velocity just outside the boundary layer, μ is the dynamic fluid viscosity, and ρ is the solution density.

Mass transport simulations were carried out during the etching, submerged rinsing, and spray rinsing processes using the following conditions: $w_0=1 \mu\text{m}$, $d=30 \mu\text{m}$, $r_e=1.74 \mu\text{m/hr}$, $\rho=1.1 \text{ gm/cm}^3$, $\rho_{\text{SiO}_2}=2.2 \text{ gm/cm}^3$, $\mu=0.04 \text{ Pa s}$, $\text{MW}=60.1 \text{ gm/mole}$; and using the following estimated parameters: $v=0.1 \text{ m/s}$ (during etch), $v=0.001 \text{ m/s}$ (during rinse), $v=0.01 \text{ m/s}$ (spray rinse), $\delta=11 \mu\text{m}$ (etch) and $\delta=25 \mu\text{m}$ (submerged rinse) with ultrasonic agitation. The diffusion coefficient, which was one of the most sensitive parameters, was estimated as $5 \times 10^{-8} \text{ cm}^2/\text{sec}$ based on values described for oils with similar viscosities [23].

Simulation results for the $30 \mu\text{m}$ deep crack are shown in Fig. 11 at various times and steps during the etch, rinse, and spray rinse processes for Sample G4. At time $t=0$, the crack is very narrow and the reaction product concentration is zero everywhere. During the etching process, a concentration gradient of the reaction product in the boundary layer forms and the crack width increases (see concentration profiles at t_1 , t_2 , and t_3 in Fig. 11). Note the overall concentration within the boundary layer ($\sim 10^4 \text{ mol/m}^3$) is very high at this stage due to a relatively small diffusion coefficient and a relatively large source of reaction products coming from the etching surface. When the sample is transferred to the rinse tank at time t_3 , it takes a finite thickness of reaction fluid with it which is transferred into the water rinse tank as the starting condition. During the submerged rinse, the crack shape does not change (i.e., no moving boundary), and the reaction product has sufficient time to be removed from the boundary layer as can be seen in the concentration profiles at times t_4 and t_5 . However, because the tank size is finite, all the reaction product will evenly distribute into the rinse tank to C_∞ which is $\sim 6 \text{ mol/m}^3$. Note the solubility of $(\text{NH}_4)_2\text{SiF}_6$ is 18 mol/m^3 for 20:1 BOE and 215 mol/m^3 for 6:1 BOE (3x diluted). Also, using the micrograph shown in Fig. 7 and estimating the volume of the precipitate, we estimate the solution during drying had a concentration of $\sim 2 \text{ mol/m}^3$. Hence, if the sample was removed from the rinse tank and allowed to dry, the concentration would be sufficient to lead to the amount of precipitation shown in Fig. 7. During the spray rinsing process, the diffusion of the reaction product from the boundary layer continues, but in this case C_∞ is much smaller and remains low since the clean water is constantly being applied. From times t_5 to t_7 , essentially all the reaction product is removed. For comparison, the concentration of cations expected in the deionized water (18 MΩ) is $\sim 10^{-3} \text{ mol/m}^3$.

For short etch times, the rinse is expected to be diffusion limited as described in the model above. Hence as the depth of crack increases, the effective time for reaction product removal

would increase. This is illustrated in Fig. 12 which shows simulations of the average reaction product concentration as a function of submerged rinse time for various crack depths. From previous studies, the average depth of the scratch is related to the scratch width as [2,17]:

$$w_o \cong 0.35d_o \quad (15)$$

Hence, this implies that as the width of the scratch increases, the depth increases and then mass transport times increases. This analysis is consistent with the results that damage threshold generally decreases with increasing scratch width as shown in Fig. 3.

4.2.2 Ultrasonic/Megasonic Agitation During Etch and Rinse

Ultrasonic/megasonic frequency fluid agitation is commonly used for removing particles from the surfaces of components. The non-elastic nature of the fluid allows for cavitation (rapid formation and subsequent implosion of bubbles due to oscillating pressure created by sound waves from a transducer source). The bubble implosion results in a shock wave providing fluid momentum near the component surface forcing particles away. The bubble diameter (d_b), which determines both the bubble proximity to the component surface and the extent of fluid response, is given by:

$$d_b = \frac{1}{\pi f} \sqrt{\frac{3 \kappa p_o}{\rho}} \quad (16)$$

where f is the transducer frequency, p_o is the hydrostatic pressure (1 atm), ρ is fluid density (1 gm/cm³), and κ is the polytropic index (~1.3 for water at room temperature). Since the velocity of the fluid just at the surface is zero, the fluid agitation and hence the mass transport near a surface is limited by boundary layer theory. This acoustic boundary layer thickness (δ_{ac}) is described as [24]:

$$\delta_{ac} = \sqrt{\frac{\mu}{\pi f \rho}} \quad (17)$$

where μ is the viscosity of the fluid.

Figure 13 shows the calculated bubble diameter and acoustic boundary layer as a function of frequency (using Eqs. 16 and 17). From 20 KHz to 1300 KHz, the bubble diameter decreases from 315 μ m to about 5 μ m, and the acoustic boundary layer thickness decreases from 4 μ m to 0.5 μ m. The higher frequency has the advantage of removing smaller particles due to the reduction of the acoustic boundary layer. When removing dissolved species instead of particles, as in the case of acid etching, the reaction product will initially be removed by diffusion within the diffusive boundary layer. Although the quantitative determination of the diffusive boundary

layer thickness is more complex, it is expected to be proportional to the acoustic boundary layer thickness and scale in a similar manner with frequency.

Using the mass transport model described in Section 4.2.1, simulations of the submerged rinse process for varying degrees of agitation are shown in Fig. 14. In these simulations, a 30 μm crack is etched for 30 min and is then rinsed in a submerged tank. The static rinse was simulated by using a large boundary layer ($\delta \sim 1$ mm) and setting the mass transport coefficient k_c to zero. The other cases using various frequency agitations were simulated by using the acoustic boundary layer thickness (Eq. 17) and by adjusting the velocity of the fluid at the boundary layer. Note we have assumed that the $v \sim f^2$ [25]. The results show that an increase in frequency results in a significant increase in mass transport of the SiF_6^{2-} reaction product. These calculations are consistent with the experimental results showing the damage threshold of the etched surface crack increases significantly with addition of agitation (see Fig. 3). Although the simulations above had to rely on engineering approximations of the initial velocity near the boundary layer and the viscosity of the reaction product rich fluid, the scaling behavior observed appears to be valid.

4.2.3 Drying

As shown in Fig. 7, the majority of the redeposit collects in the etched cracks (cusps), and, more specifically, collects preferentially just inside the perimeter of the cusps. Also, the laser damage initiation on these treated surfaces first initiates at the edge of the cusps. Collection of redeposit at this location on the surface is an important clue to the mechanism of their precipitation and provides insights for methods to prevent it from occurring.

The preferential collection of redeposit at the cusp edge is likely due to an effect analogous to a drying droplet of fluid that leaves a ring-like deposit along the perimeter (e.g., hard water stains rings or coffee ring stains) [26]. This behavior is caused by surface tension-induced fluid pinning (i.e., the areal droplet size stops decreasing with drying) which results in fluid flow toward the cusp perimeter during drying. The fluid flow is caused by a greater evaporative flux ($J(r)$) at the perimeter which scales as [26]:

$$J(r) \propto (R - r)^{-\left(\frac{\pi - 2\theta_c}{2\pi - 2\theta_c}\right)} \quad (18)$$

where R is the pinned radius or cusp radius, and θ_c is the contact angle between the fluid and substrate. Since the fluid is pinned, the radial evaporation flux gradient results in the perimeter to evaporate faster than the center causing fluid to migrate to the perimeter. Hence, this fluid flow results in both particulates in the fluid and dissolved species to migrate and collect at the perimeter of the pinned droplet.

This behavior was illustrated by dissolving food coloring in water and allowing it to dry on a previously etched scratch on fused silica. After drying, the food coloring crystals reprecipitated near the cusp perimeter (see Fig. 15) which is consistent with the mechanism described above. During drying several interesting phenomena were observed. First, the flat surface (exterior to the cusps) dried with a liquid front line that passed by and around all the cusps. Because the

liquid front was not pinned, the dissolved dye was drawn away with the liquid front and little redeposit was observed outside of the cusps. Second, any particulates observed were carried with the liquid front. If the cusp interfered with the liquid front, particles would often collect on the cusp perimeter. After the drying front passed, only the cusps were filled with fluid. Then as the water evaporated from the cusps themselves, the dye precipitated just inside the perimeter of the cusps.

Based on this mechanism, it suggests that the majority of the precipitation or redeposit occurs during drying rather than during etching or rinsing. The final concentration of the dissolved reaction products dictates the extent of redeposit and hence the laser damage resistance of the optic. Hence to minimize precipitation or redeposit, it is important to minimize the concentration of the reaction products in the solution at the drying stage by using an effective agitated submerged rinse and spray rinse.

4.3 Amount Etched and Damage Performance

In addition to improving the laser damage threshold of scratches by increasing the reaction product solubility and mass transport, increase in damage threshold also resulted from increasing the etched amount to $>20\text{ }\mu\text{m}$ (see Figs. 3 and 4a). Based on previous studies [14], the intrinsic absorbing precursor on fracture surfaces is present only on a thin layer near the fracture surface (10-100 nm), hence the relatively large etched amounts needed for achieving the high laser damage thresholds were initially surprising. There are several proposed mechanisms to explain the need for the relatively large etched amounts: 1) the light intensification due to reflections and interference near the cusp decreases with etched amount due to change in cusp shape increasing the effective damage threshold; 2) the lateral cracks, for which the acid appears to have a more difficult time penetrating, needs to be etched through with greater etched amounts to eliminate the absorbing fracture surface; and 3) the trailing indent cracks (which form cusps) need to open up sufficiently with etched amount to allow for increased mass transfer rates of reaction product away from the surface. The latter two are discussed in more detail below.

Lateral cracks, in addition to the trailing indent cracks, are often observed on scratches [17]. Figure 16a shows the presence of lateral cracks on an etched scratch observed on sample F3. Figure 16b shows the corresponding photoluminescence image of the same etched scratch, where the lateral cracks still have significant photoluminescence suggesting that the acid did not effectively penetrate and remove the absorbing defect layer. In contrast, both the morphology and the lack of photoluminescent signal from the trailing indent cracks confirm acid penetration and etching of these fracture surfaces. Because the trailing indent fracture surface is largely perpendicular to the lateral fracture surface, the lateral crack can be eliminated by etching open the trailing indent crack sufficiently to etch through the lateral crack. In the case shown in Fig. 16, this suggests $\sim 10\text{ }\mu\text{m}$ of additional etching would be required. For other scratches, it is possible that larger lateral cracks are present which would require even more material removal to completely mitigate the scratch.

Another hypothesis to explain the need for large etched amounts ($>20\text{ }\mu\text{m}$) is that the removal of the reaction product from a wider crack (etched more) is faster than from a narrow crack (etched less). The morphology of the scratch itself changes significantly with the amount etched where

the width and length of the trailing indent cracks increase as illustrated in Fig. 17. In the 2D mass transport model described above, the transport within the boundary layer is purely diffusive. With this assumption, the reaction products of a narrow crack and wider crack will be removed at nominally the same rate for a given crack depth. However, expanding the 2D mass transport model to include hydrodynamic flow due to advection within the boundary layer, we find the reaction product removal rate to depend strongly on the opening of the crack (see below). In this case, the concentration of the reaction product (c) within the boundary layer (which includes the interior of the etched crack) as a function of etch time and position is now given by:

$$\frac{\partial \vec{v}}{\partial t} + \vec{v} \cdot \nabla \vec{v} = \left(\frac{\mu}{\rho} \right) (\nabla \cdot \nabla) \vec{v} \quad (19)$$

$$\frac{\partial c}{\partial t} + \vec{v} \cdot \nabla c = \nabla \cdot (D \nabla c) \quad (20)$$

where μ is the dynamic fluid viscosity, ρ is the fluid density, \vec{v} is the vector fluid velocity and D is the diffusivity of the etch product.

Using the advection and diffusional 2D mass transport model, the calculated reaction product concentration during the submerged rinse as a function of rinse time for a 30 μm deep crack of various widths (i.e., various amounts etched) is shown in Fig. 18a. The concentration decreases exponentially with etch time for all widths. As the crack width increases (or the amount etched increases), the time constant for reaction product removal decreases. For crack widths between 20-30 μm , the time constant of removal is approximately the same as for a flat surface. In other words, at these widths the opening of the crack is sufficient to allow advection transport effectively reducing the diffusive boundary layer equivalent to that of a flat surface. Fig. 18b illustrates this by showing the calculated vector flux of the reaction product which is increased within the wider crack. These calculations support the hypothesis that the improved damage thresholds are achieved with etched amounts $>20 \mu\text{m}$ because the morphology (namely width) of the crack opens up, thus enhancing mass transport rates during the rinsing process. In addition, the calculations predict the benefit of etching is maximized at 20-30 μm removal, which is consistent with the experimental data shown in Fig. 4a.

5. CONCLUSIONS

Aqueous fluoride-based etching processes have been shown to significantly improve both the small beam and large beam laser damage threshold of scratched fused silica surfaces. The etch process improvements are based on removing or preventing the three identified precursors (fracture surfaces, impurities in the polish layer, and particularly redeposition of reaction products). Redeposition was reduced by: 1) increasing the solubility of the reaction products through modifications in the acid composition and impurity cation reduction; and 2) increasing the mass transport of reaction products away from the etched surface through agitated etching & rinsing, aggressive spray rinsing, and optimized etched amounts. A 2D finite element crack-etching and rinsing mass transport model (incorporating diffusion and/or advection) was used to

predict reaction product concentration, whose predictions are consistent with the experimentally observed process trends. This patented etch process [16] (called Advanced Mitigation Process or AMP) is now being used to treat fused silica optics in high-peak power laser optics used in the National Ignition Facility.

ACKNOWLEDGEMENTS

The authors would like to thank the Advanced Mitigation Process (AMP) production team members (R. Aboud, B. Bell, T. Biesiada, B. Bishop, D. Coufal, B. Edwards, S. Frieders, R. Gutierrez, R. Hawley, S. Humphreys, T. Leever, T. Marsh, L. Minjares, B. Rainey, G. Robitaille, J. Rodriguez, D. Van Lue, S. Whitehouse) and OSL laser & damage testing group (M. Bolourchi, H. Bigman, D. Cross, G. Donohue, B. Hollingsworth, Z. Liao, R. Luthi, J. Prior, F. Ravizza, G. Guss, R. Negres, J. Adams, T. Weiland, P. Wegner, P. Whitman) for their efforts. This work was performed under the auspices of the U.S. Department of Energy by Lawrence Livermore National Laboratory under contract DE-AC52-07NA27344 under the LDRD program.

REFERENCES

1. J. Menapace, J. Peterson, B. Penetrante, P. Miller, T. Parham, M. Nichols, "Combined advance finishing and UV laser conditioning process for producing damage resistant optics," U.S. Patent 6920765 (July 26, 2005).
2. T. Suratwala, L. Wong, P. Miller, M. Feit, J. Menapace, R. Steele, P. Davis, D. Walmer, "Sub-surface mechanical damage distributions during grinding of fused silica," *Journal of Non-Crystalline Solids* 352 (2006) 5601.
3. P. Miller, T. Suratwala, L. Wong, M. Feit, J. Menpace, P. Davis, and R. Steele, "The distribution of sub-surface damage in fused silica," *SPIE* 5991 (2005).
4. M. Nichols, D. Aikens, D. Camp, I. Thomas, C. Kiikka, L. Sheehan, M. Kozlowski, "Fabrication of an Optical Component." U.S. Patent 6099389 (August 8, 2000).
5. L. Hackel, A. Burnham, B. Penetrante, R. Brusasco, P. Wegner, L. Hrubesh, M. Kozlowski, M. Feit, "Method for producing damage resistant optics," U.S. Patent 6518539 (February 11, 2003).
6. J. Britten, L. Summers, "Multiscale, multifunction diffractive structures wet etched into fused silica for high-laser damage threshold applications," *Applied Optics* 37(30) 7049 (1998).
7. L. Wong, T. Suratwala, M. D. Feit, R. Steele, "The Effect of HF/NH₄F Etching on the Morphology of Surface Fractures on Fused Silica," *Journal of Non-Crystalline Solids* 355 (2009) 797.

8. G. Spierings, "Wet chemical etching of silicate glasses in hydrofluoric acid based solution", *J. Mater. Sci.* 28 (1993) 6261.
9. J. Yoshiyama, F. Genin, A. Salleo, I. Thomas, M. Kozlowski, L. Sheehan, I. Hutcheon, D. Camp, "Effects of polishing, etching, cleaving, and water leaching on the UV laser damage of fused silica," *SPIE* 3244 (1998) 334.
10. C. Battersby, L. Sheehan, M. Kozlowski, "Effects of wet processing on laser induced damage of fused silica surfaces," *SPIE* 3578 446 (1999).
11. M. Norton, I. Hrubesh, B. Molander, "Damage growth on etched fused silica," NIF-0047009 (April 12, 2000).
12. L. Hrubesh, M. Norton, B. Molander, P. Wegner, M. Staggs, S. Demos, J. Britten, L. Summers, E. Lindsey, M. Kozlowski, "Chemical etch effects on laser induced damage growth in fused silica," *SPIE* 4347 (2001) 553.
13. Ph. Bouchut, P. Garrec, C. Pelle "Wet etching for the mitigation of laser damage growth in fused silica", *SPIE* 4932 (2003) 103-111.
14. P. Miller, T. Suratwala, J. Bude, J. Menapace, N. Shen, W. Steele, T. Laurence, M. Feit, and L. Wong, "Identification of laser damage precursors in fused silica," *SPIE* 7504 (2009) X1-11.
15. T. Laurence, J. Bude, N. Shen, T. Feldman, P. Miller, W. Steele, T. Suratwala, "Metallic-like photoluminescence and absorption in fused silica surface flaws," *Applied Physics Letters* 94 (2009) 151114.
16. P. Miller, T. Suratwala, J. Bude, N. Shen, W. Steele, T. Laurence, M. Feit, L. Wong, "Methods for globally treating silica optics to reduce optical damage," US Patent application 12572220, October 1, 2009.
17. T. Suratwala, P. Miller, M. Feit, J. Menapace, "Scratch Forensics," *Optics & Photonics News*, September 2008, 12.
18. J. Hue, et. al., "R-on-1 automatic mapping: a new tool for laser damage testing" *SPIE* 2714 (1996) 90-101.
19. M. Nostrand, et. al. "A large aperture, high energy laser system for optics and optical component testing," *SPIE* 5273 325.
20. C. W. Carr, M. D. Feit, M. C. Nostrand and J.J. Adams, *Meas. Sci. Technol.* **17**, (2006) 1958-1962.

21. M. Feit, T. Suratwala, L. Wong, W. Steele, P. Miller, J. Bude, "Modeling wet chemical etching of surface flaws on fused silica," SPIE 7504 (2009) L1-13.
22. J. Welty, C. Wicks, R. Wilson, G. Rorrer, Fundamentals of Momentum, Heat, and Mass Transfer, 4th Edition, John Wiley & Sons (2001) Chapter 28.
23. M. Hermansson, "Self-Diffusion of Oil in Lubricating Greases by NMR," *JSL* 13-3 288 .
24. G. L. Gooberman, *Ultrasonics Theory and Application*, Hart Publishing Company Inc, New York, NY (1969).
25. C. Ekhart, "Vortices and streams caused by sound waves," *Physical Review* (73) 1 (1948) 68-76.
26. R. Deegan, O. Bakajin, T. Dupont, G. Huber, S. Nagel, T. Witten, "Capillary flow as the cause of ring stains from dried liquid drops," *Nature* 389 (1997) 82.

Table 1: Summary of etching parameters and damage test results for scratched fused silica samples.

Sample	Acid	Comp/ Conc	Etch Parameters			Rinse Parameters			Amount Removed (μm)	Small Beam laser initiation ⁴ (J/cm^2)
			Agitation Freq. (KHz)	Etch Time ¹ (min)	Temp ($^{\circ}\text{C}$)	Agitation Freq (KHz)	Submerged Time (min)	Spray Rinse Time (min)		
A1	No etch	na	na	na	na	na	na	5	0.0	7.7\pm0.3
B1	BOE	20:1	static	5	70	40	30	5	2.6	4.6 \pm1.8
B2	BOE	20:1	static	30	25	40-270	30	5	2.6	7.5 \pm1.2
C1	BOE	20:1	40-270	30	30	40	30	5	1.4	10.3 \pm1.5
C2	BOE	20:1	40-270	30	22	40	30	5	2.2	15.7 \pm3.5
C3	BOE	20:1	40-270	30	22	430-1300	30	5	2.7	13.6 \pm0.6
C4	BOE	20:1	430-1300	30	27	40-270	30	5	2.1	17.3 \pm1.7
C5	BOE	20:1	430-1300	30	55	40-270	30	5	2.3	18.2 \pm2.5
C6	BOE	20:1	430-1300	120	30	40-270	30	5	6.3	15.4 \pm2.0
D1	BOE	6:1	430-1300	60	22-32	80-270	30	5	13.7	15 \pm4.3
D2	BOE	6:1	430-1300	90	22-32	80-270	30	5	18.0	17.3 \pm3.0
D3	BOE	6:1	430-1300	120	22-32	80-270	30	5	24.0	16.8 \pm3.0
D4	BOE	6:1	430-1300	135	22-32	80-270	30	5	30.4	16.6 \pm2.8
E1	BOE	6:1(3x dil) ²	static	30	25	spray	5	5	1.2	8.8 \pm1.5
E2	BOE	6:1 (3x dil)	static	30	25	spray	5	5	1.2	13.3 \pm0.5
F1	BOE	6:1 (3x dil)	430-1300	5	30	40-270	30	5	0.4	20.4 \pm2.72
F2	BOE	6:1 (3x dil)	430-1300	15	30	40-270	30	5	1.0	18.5 \pm2.6
F3	BOE	6:1 (3x dil)	430-1300	30	25	40-270	30	5	1.4	19.4 \pm2.6
F5	BOE	6:1 (3x dil)	430-1300	60	25	40-270	30	5	2.5	21.5 \pm3.0
F6	BOE	6:1 (3x dil)	430-1300	90	25	40-270	30	5	3.7	15.6 \pm2.1
F7	BOE	6:1 (3x dil)	430-1300	120	30	40-270	30	5	7.0	13.4 \pm1.2
F8	BOE	6:1 (3x dil)	430-1300	300	25	80-270	30	30	16.3	12 \pm1.0
F9	BOE	6:1 (3x dil)	430-1300	3 x 10	25	270	3	5	1.4	19.7 \pm1.6
F10	BOE	6:1 (3x dil)	430-1300	9 x 10	25	270	30	5	5.0	19.7 \pm0.7
G1	BOE ³	6:1 (3x dil)	430-1300	30	25	40-270	30	30	1.0	15.6 \pm1.2
G2	BOE ³	6:1 (3x dil)	430-1300	150	25	40-270	30	30	5.7	30.7 \pm2.0
G3	BOE ³	6:1 (3x dil)	430-1300	360	25	40-270	30	30	11.1	30.7 \pm1.3
G4	BOE ³	6:1 (3x dil)	430-1300	450	25	40-270	30	30	27.0	41.6 \pm2.5
H1	HF	5%	static	150	25	80-270	30	30	4.4	13.1 \pm1.8
H2	HF	5%	static	300	25	80-270	30	30	9.0	15.35 \pm1.7
H3	HF	5%	static	645	25	80-270	30	30	15.8	24.22 \pm1.3
H4	HF	5%	static	810	25	80-270	30	30	20.0	33.25 \pm2.3
H5	HF	5%	430-1300	300	25	80-270	30	30	20.6	37.7 \pm3.3
H6	HF	10%	static	130	22	80-270	30	30	8.7	23.9 \pm6.2
H7	HF	10%	static	200	22	80-270	30	30	14.3	32.2 \pm6.2
H8	HF	10%	40-270	5	70	40	30	30	2.7	11.2 \pm1.3
H9	HF	49%	static	10	25	80-270	30	30	0.3	16.4 \pm1.9
H10	HF	49%	static	30	25	40-270	30	30	35.8	41.1 \pm2.5
H11	HF	49%	430-1300	3	25	80-270	30	5	6.6	16.4 \pm2.1
H12	HF	49%	430-1300	10	25	80-270	30	5	20.0	34.2 \pm3.8
H13	HF	49%	430-1300	30	25	40-270	30	5	53.0	36.25 \pm2.3

na = not applicable; ¹Etch in some cases was performed in multiples (for example F9 was etched 3 times for 10 minutes each); ²Acid was doped with 500 ppm by weight of NaCl; ³G series samples were prepared in a Class 100 cleanroom; ⁴Reported as the average and standard deviation for scratch between 20-30 μm in width

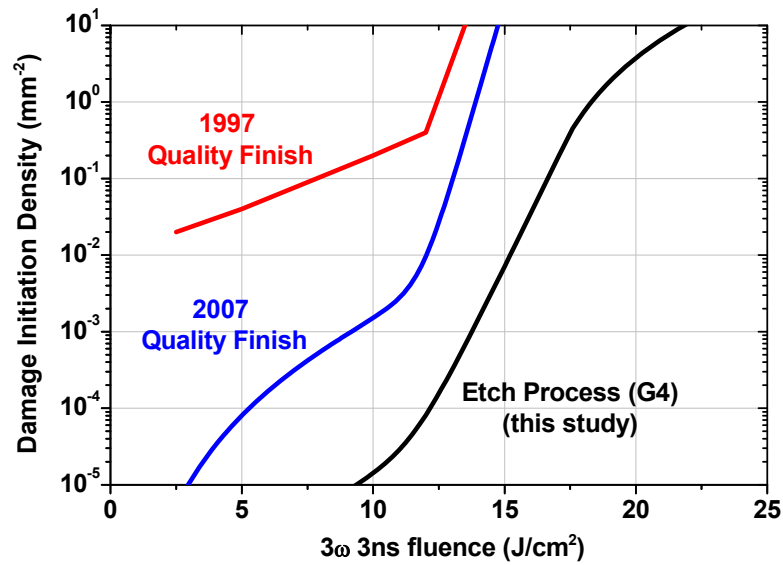


Figure 1: Laser damage initiation density of various fused silica finishing processes and a post processing acid etch treatment.

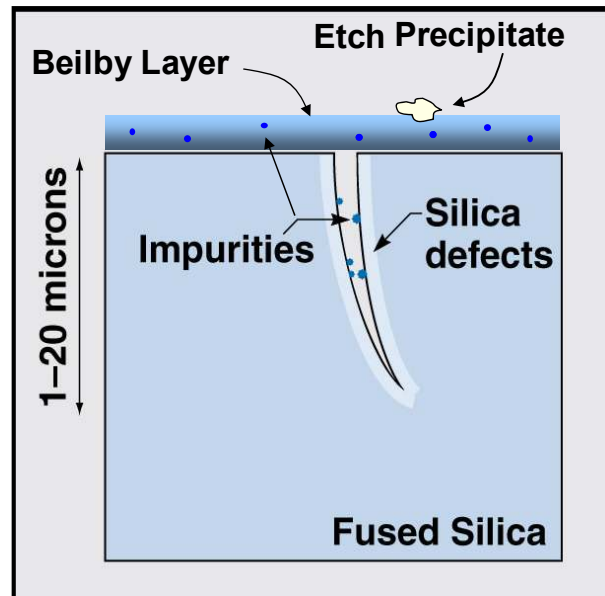


Figure 2: Schematic illustration of known absorbers on fused silica surfaces that lead to low fluence ($<45 \text{ J/cm}^2$) laser initiation (351 nm, 3ns). The absorbers are impurities in the Beilby polishing layer or cracks, the intrinsic silica defects on fracture surfaces (i.e. scratches) and redeposit of silica due to etching or laser treatment processes.

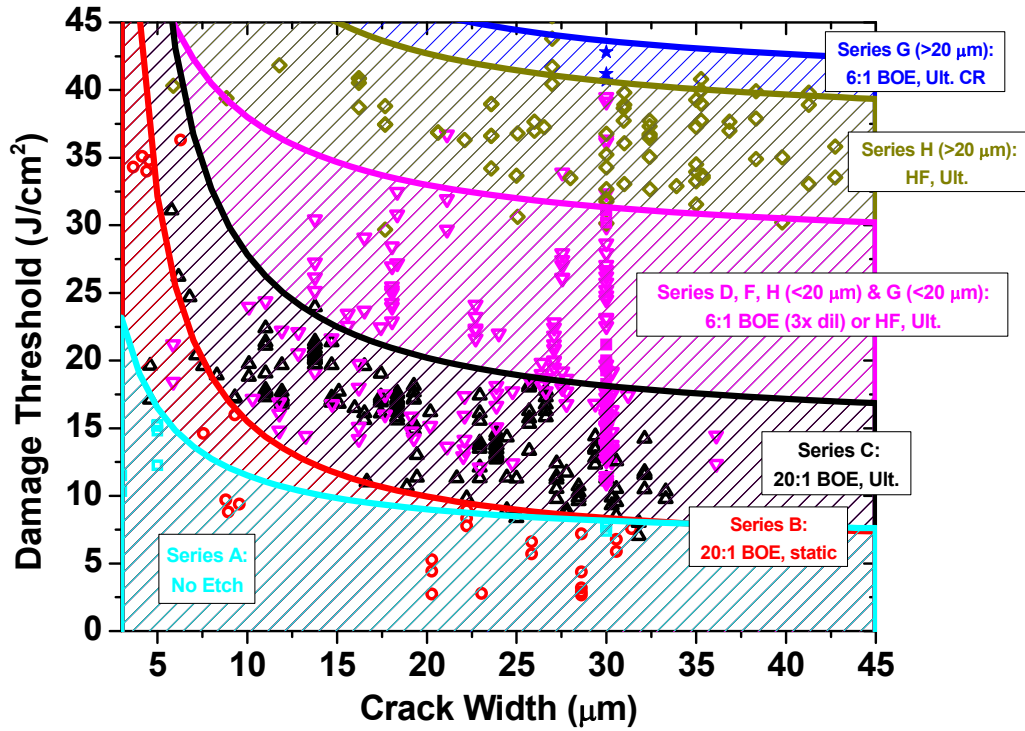
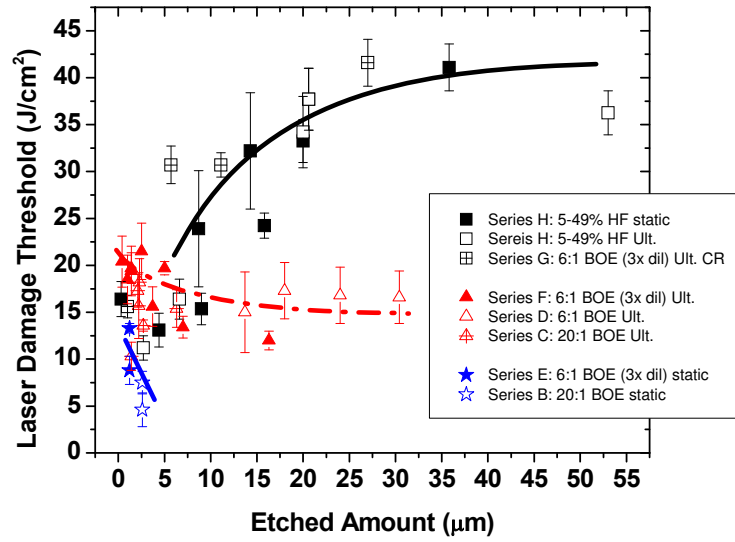
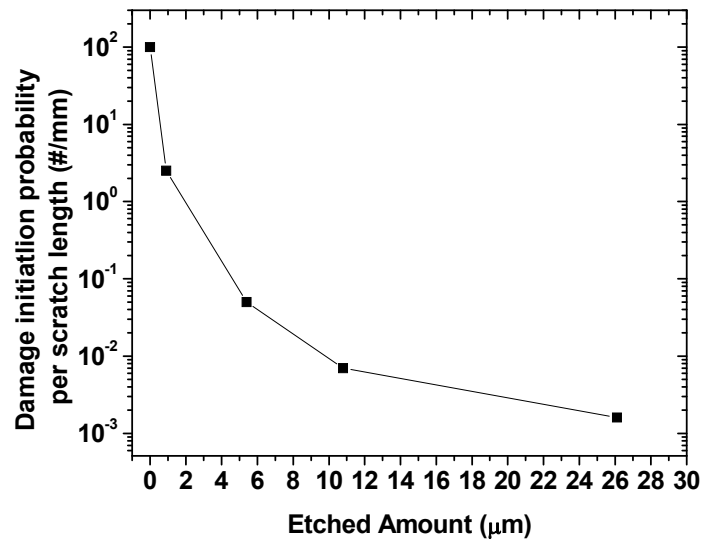


Figure 3: Summary of small beam laser damage test results as a function of the width of the scratch for various series of etch processes described in Table 1. The solid lines represent and upper bound of the laser damage threshold for the series of processes described by the label in the plot. (Ult.= ultrasonic or megasonic rinsed used; CR= processed in a cleanroom; <20 μm= less than 20 μm removed during etch; >20 μm = greater than 20 μm removed during etch).

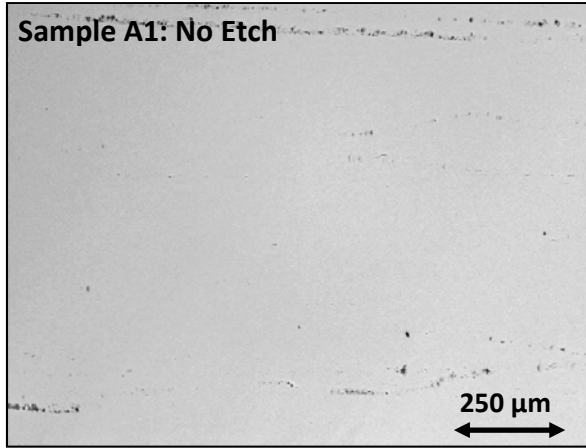


(a)

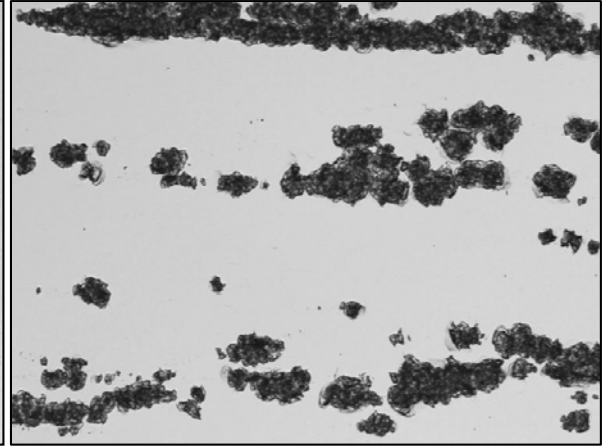


(b)

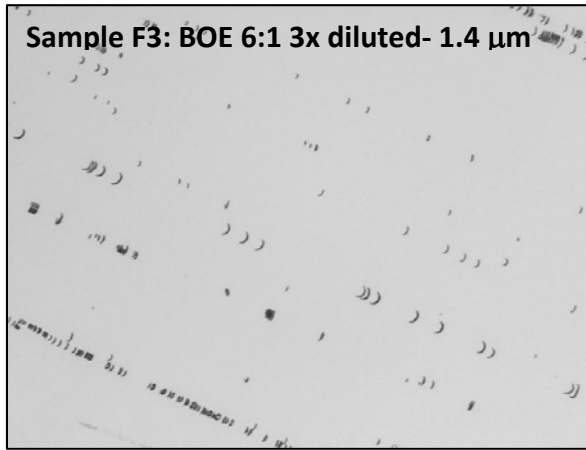
Figure 4: (a) Small beam laser damage initiation fluence (355 nm) as a function of the etched amount for various etchants and process routes. Trend lines are drawn as a guide for the eye. (b) Large beam laser damage initiation probability (351nm, 12 J/cm²) as a function of etched amount for Samples G1-G4.



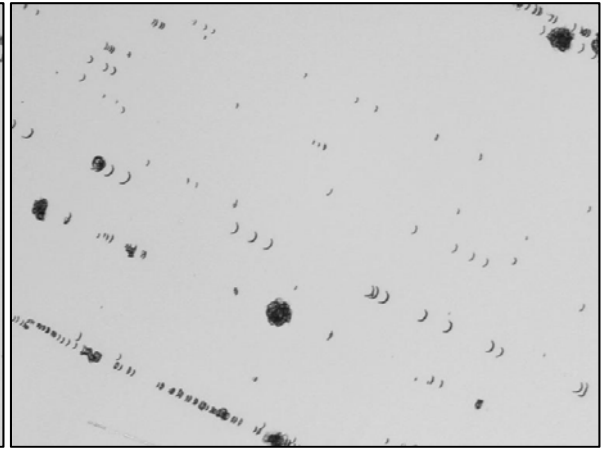
(a)



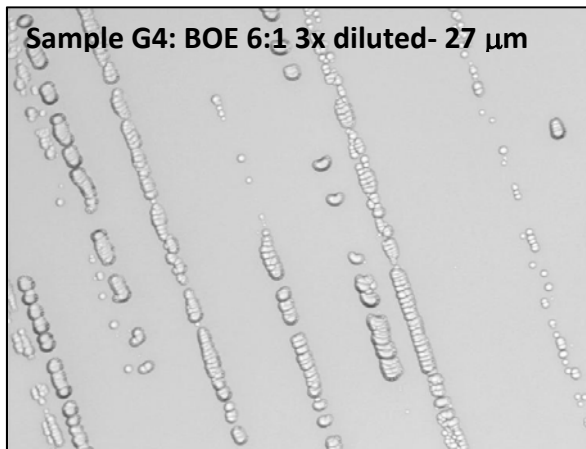
(b)



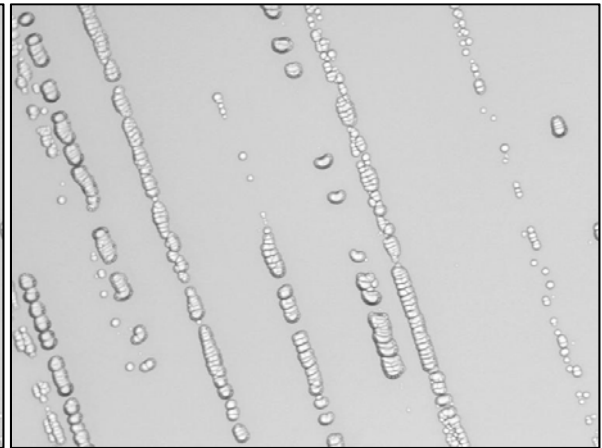
(c)



(d)



(e)



(f)

Figure 5: Optical micrographs of scratches generated on fused silica before and after being laser shot at 8,10 and 12 J/cm² (3 cm beam, 3 ns, 351 nm) for (a-b) Sample A1, (b-c) Sample F3, and (d-e) Sample G4.

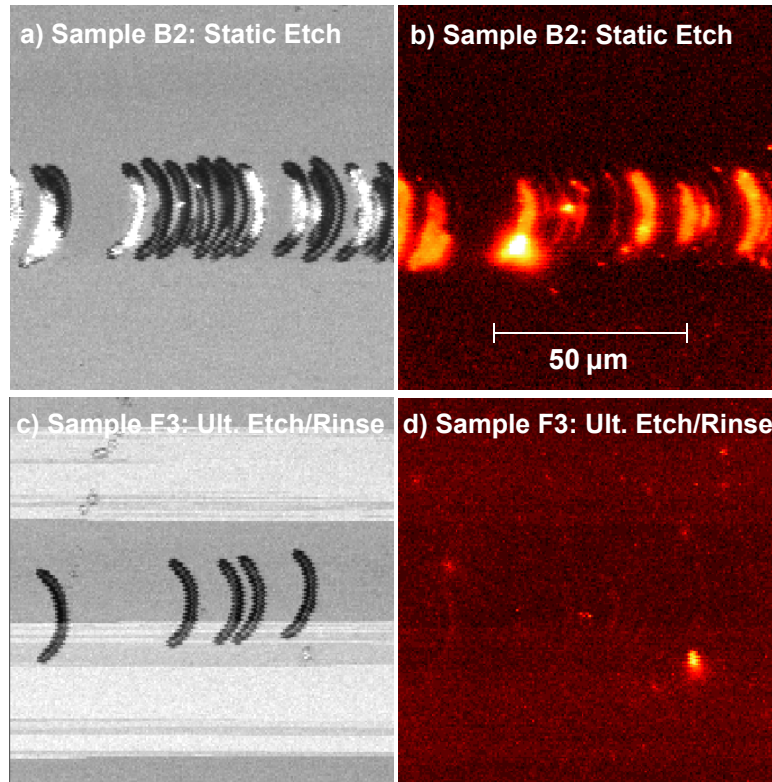


Figure 6: (a) Image of scratch on fused silica sample B2 processed without agitation during etching; (b) Photoluminescence image of same scratch on sample B2; (c) Image of scratch on fused silica sample F3 processed with agitation during etching; (d) Photoluminescence image of same scratch on sample F3.

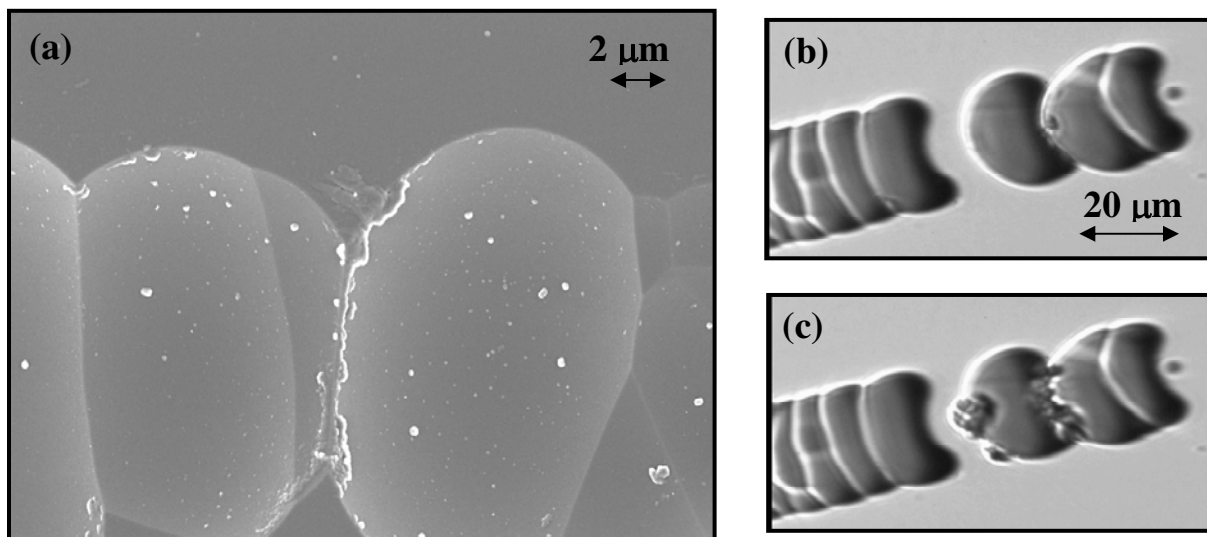


Figure 7: (a) SEM image of precipitate that is sometimes observed at the edges of etched open scratches (Sample F8). Optical micrograph of etched scratch on Sample F8 before (b) and after (c) laser damage initiation (initiation fluence= 19 J/cm^2).

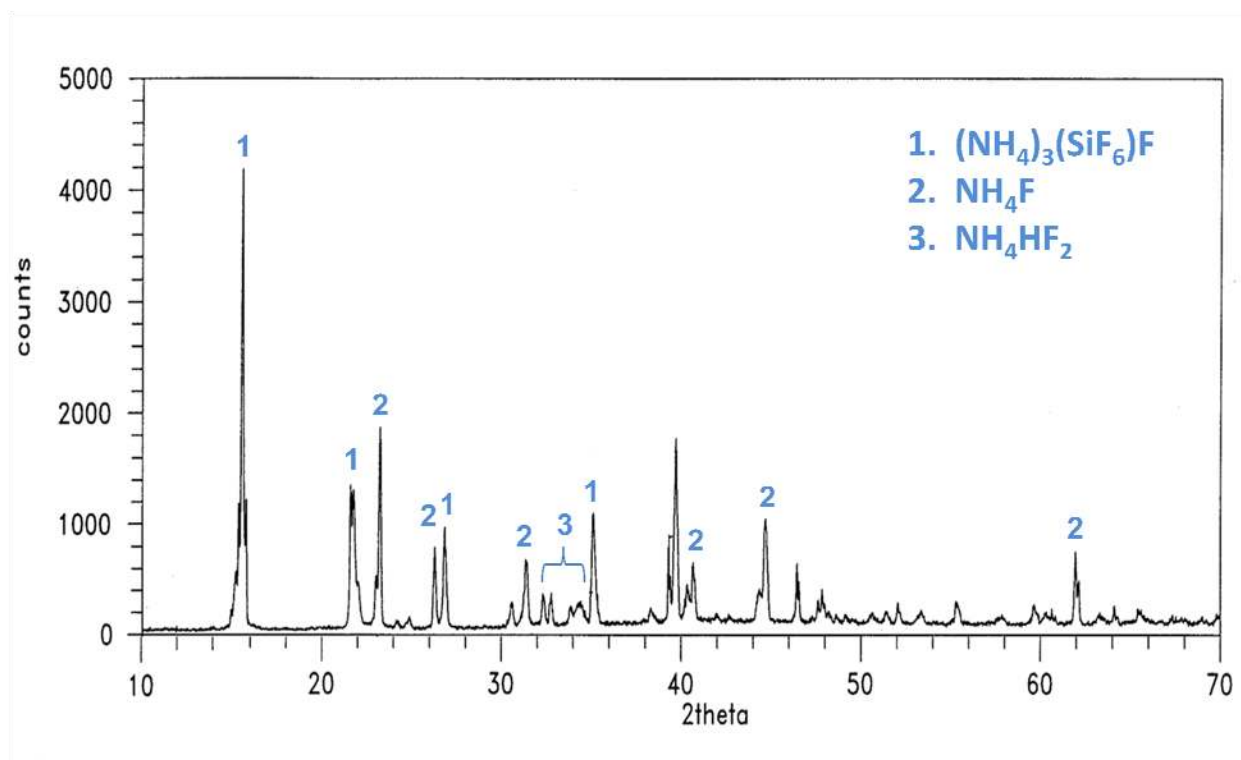
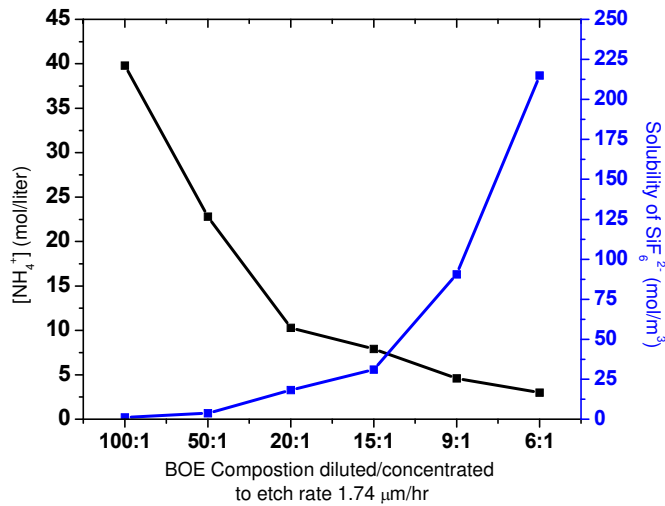
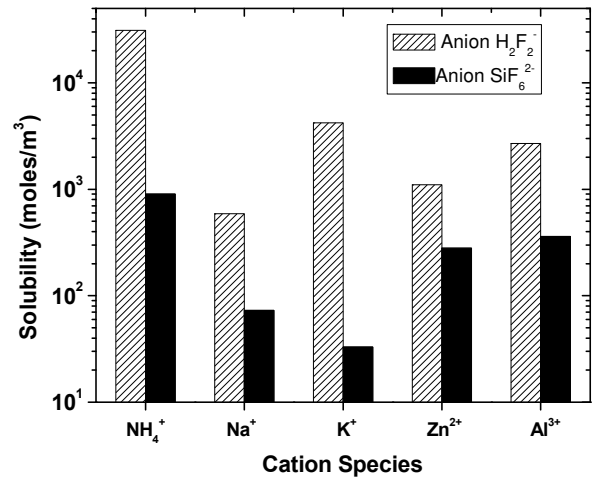


Figure 8: X-ray diffraction pattern of the crystallites formed on the silica surface after etching in BOE (sample was etched 20 hrs static in 600 ml of 20:1 BOE).



(a)



(b)

Figure 9: (a) Ammonium concentration $[\text{NH}_4^+]$ and solubility of NH_4SiF_6 (ammonium hexafluorosilicate) in various buffered-oxide-etch compositions; (b) Solubility of H_2F_2^- and SiF_6^{2-} with various cations.

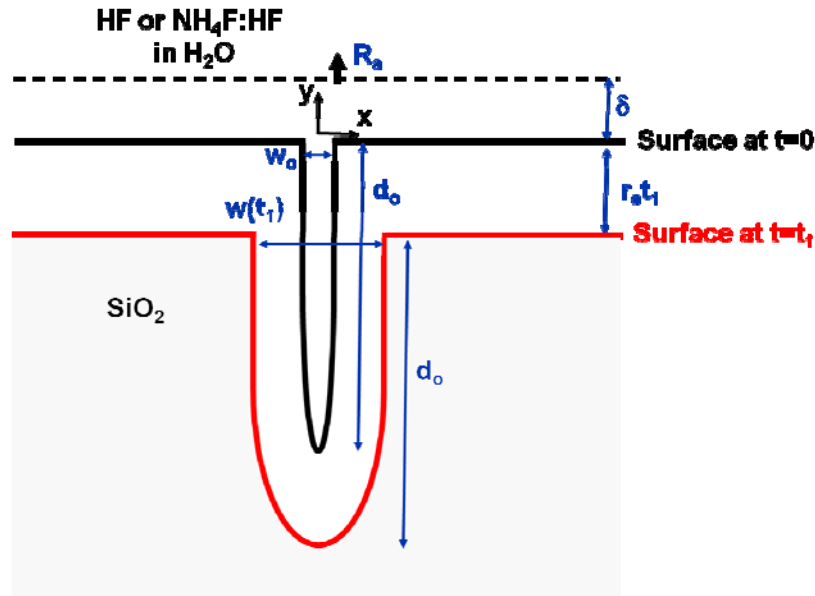


Figure 10: Schematic illustration of the 2D mass transport model for etching a crack on the surface of fused silica.

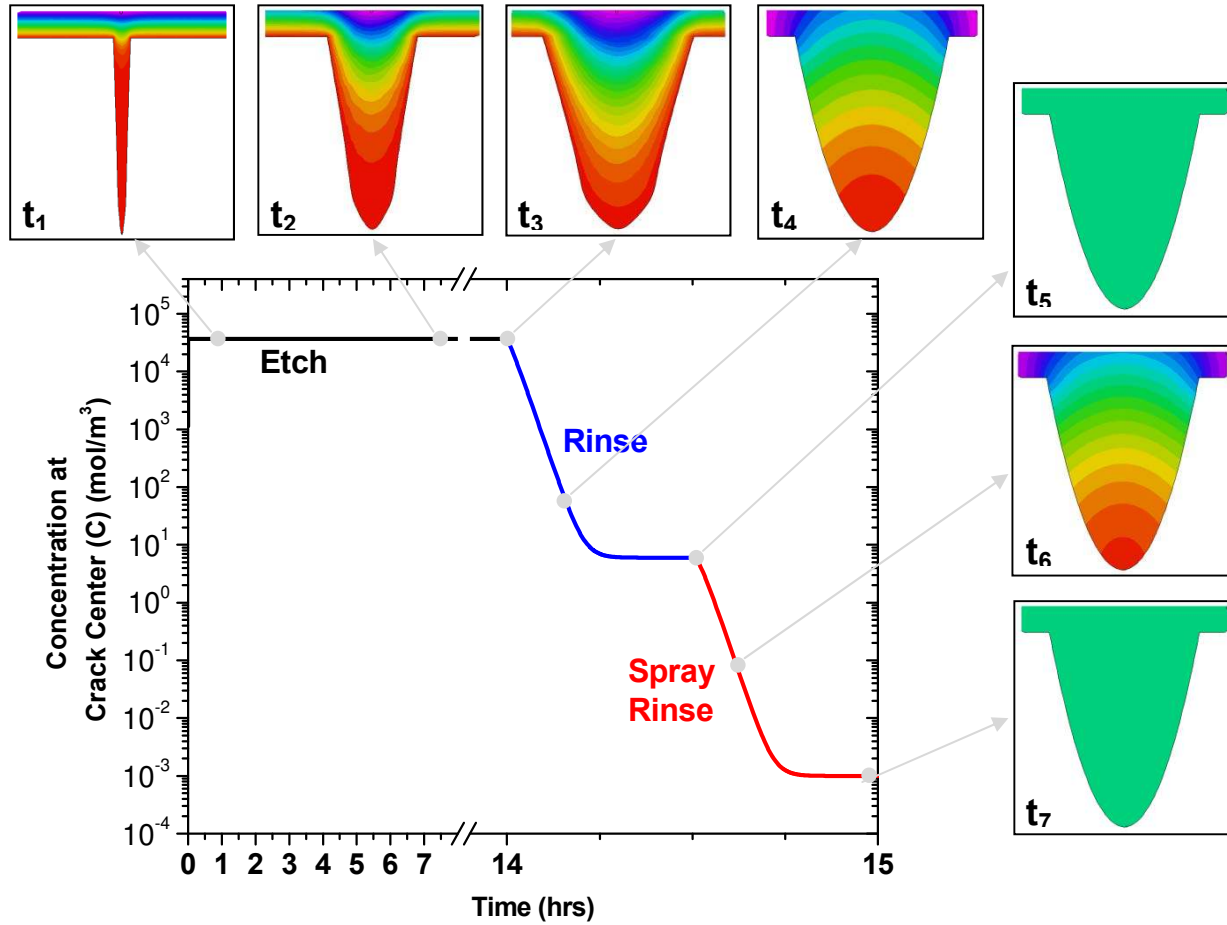


Figure 11: Calculated SiF_6^{2-} concentration as a function of process time (during etching, submerged rinsing, and spray rinsing for Sample G4) using 2D mass transport model described in section 4.2.1. For selected times, the concentration profiles of the cracks are shown. The linear contours are designated red as the maximum concentration and purple as the lowest concentration. The crack is 30 μm deep and the full horizontal scale is 60 μm . $t_1=1$ hr (max= 3.7×10^4 mol/m³; min= 2.2×10^4 mol/m³); $t_2=7$ hr (max= 3.7×10^4 mol/m³; min= 1.5×10^4 mol/m³); $t_3=14$ hr (max= 3.7×10^4 mol/m³; min= 1.0×10^4 mol/m³); $t_4=14.15$ hr (max=72 mol/m³; min=21 mol/m³); $t_5=14.5$ hr (6 mol/m³); $t_6=14.65$ hr (max=2.63 mol/m³; min=0.69 mol/m³); $t_7=15$ hr (1×10^{-3} mol/m³).

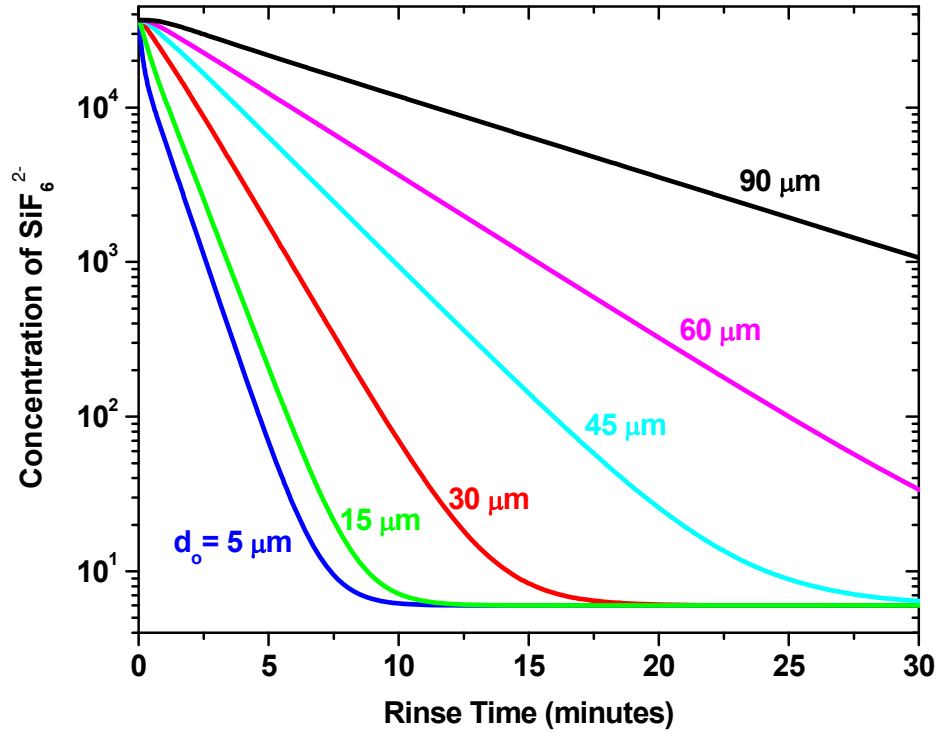


Figure 12: Calculated SiF_6^{2-} concentration at the center of an etched scratch for various scratch depths (d_o) as a function of submersed rinse time using 2D mass transport model described in Section 4.2.1.

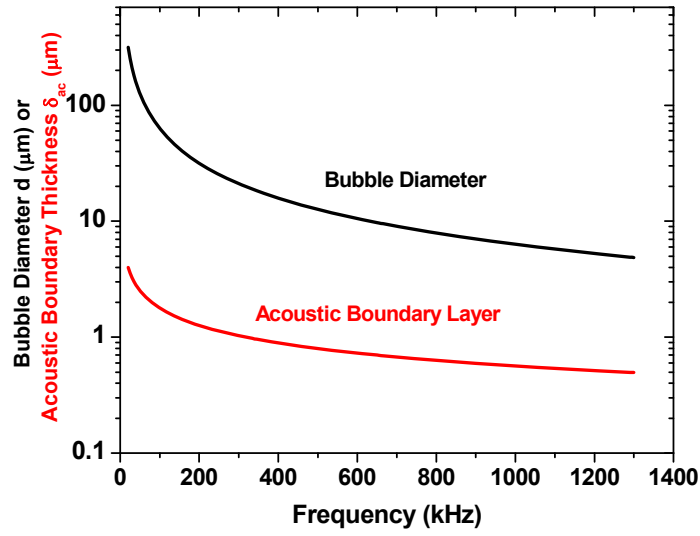


Figure 13: The bubble diameter created and the acoustic boundary layer thickness as function of ultrasonic frequency (calculated using Eqs. 16 & 17).

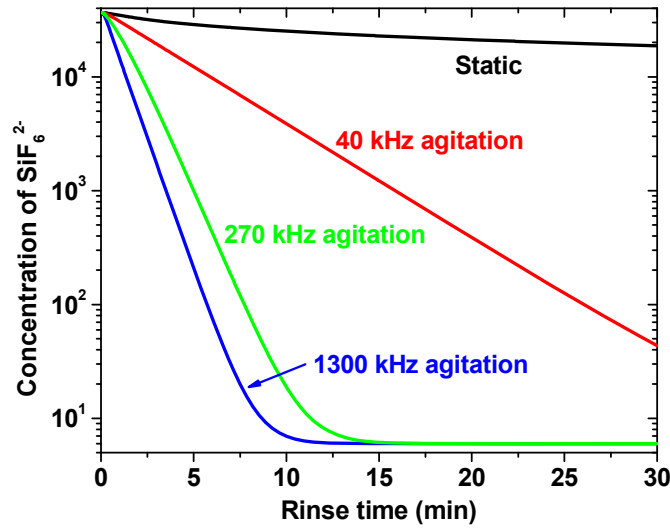


Figure 14: Calculated SiF_6^{2-} concentration at the center of an etched 30 μm deep scratch as a function of submersed rinse time. Static rinse ($\delta=1 \mu\text{m}$, $k_c=0 \text{ m/s}$); 40 kHz rinse ($\delta=56 \mu\text{m}$, $v=1 \times 10^{-4} \text{ m/s}$); 270 kHz rinse ($\delta=22 \mu\text{m}$, $v=4 \times 10^{-3} \text{ m/s}$); 1300 kHz ($\delta=10 \mu\text{m}$, $v=0.1 \text{ m/s}$).

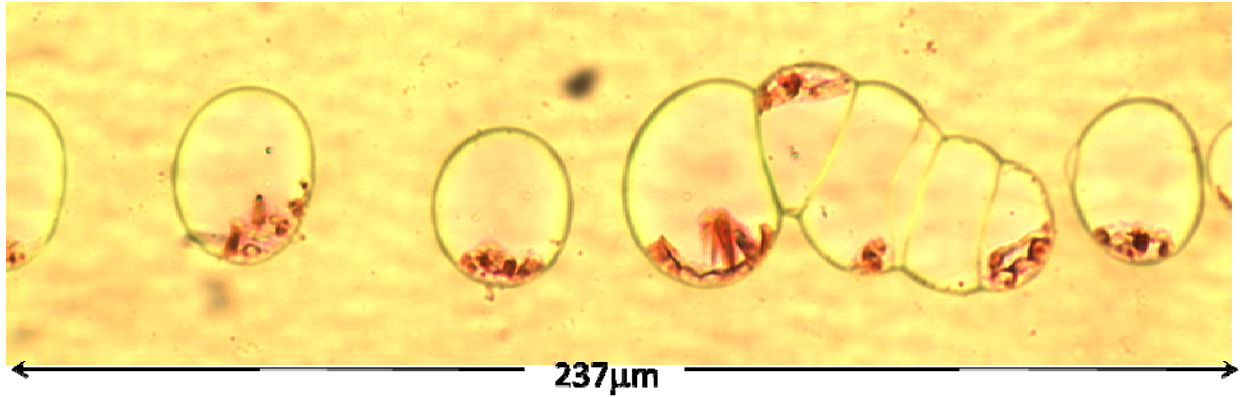


Figure 15: Optical micrograph of an etched scratch after placing a drop of dilute red food coloring in water and letting it air dry.

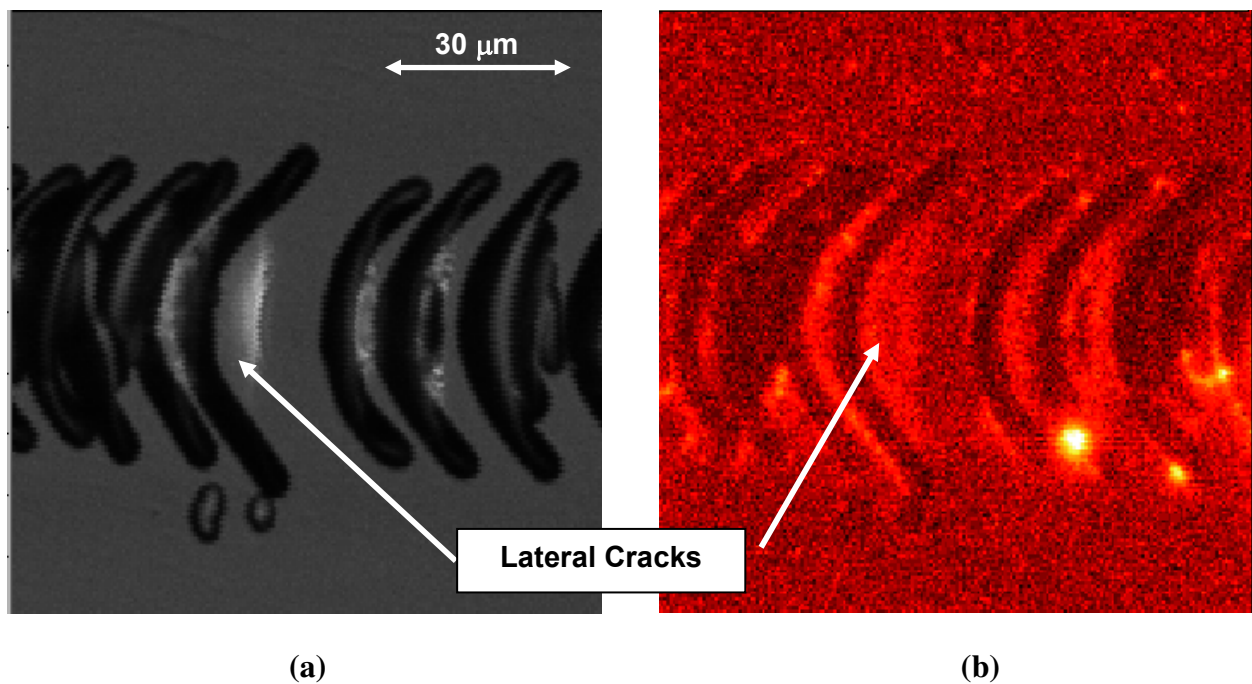


Figure 16: (a) Optical micrograph of a scratch on sample F3; (b) Photoluminescence image of the same scratch. This scratch contains lateral cracks where the etchant does not appear to penetrate well to observe PL after etching.

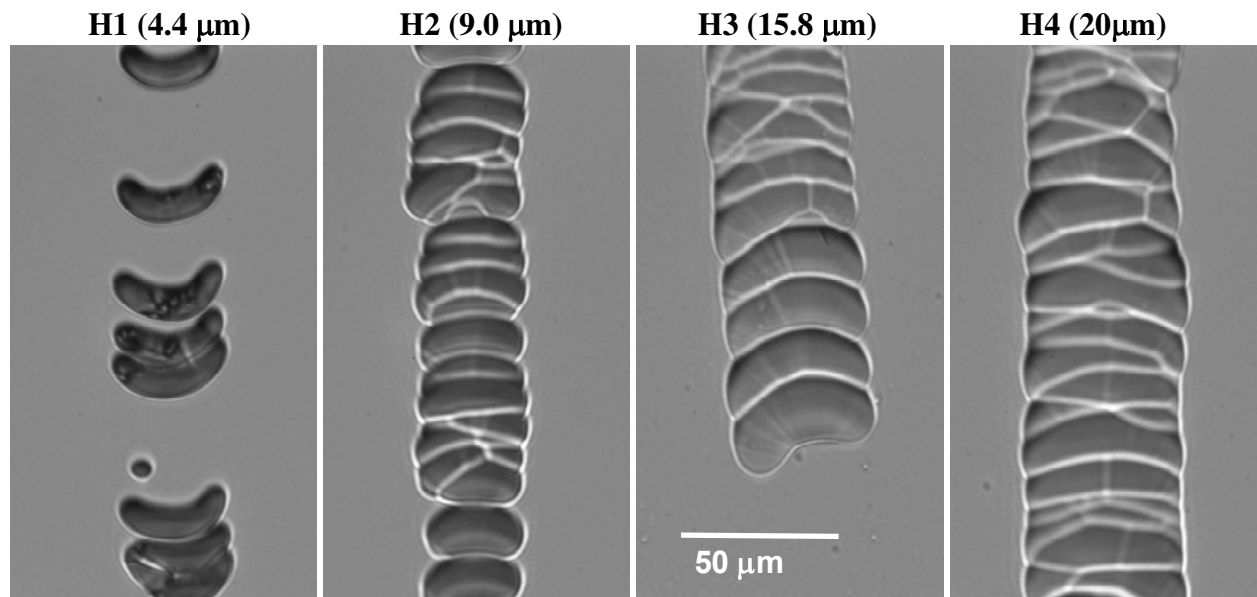
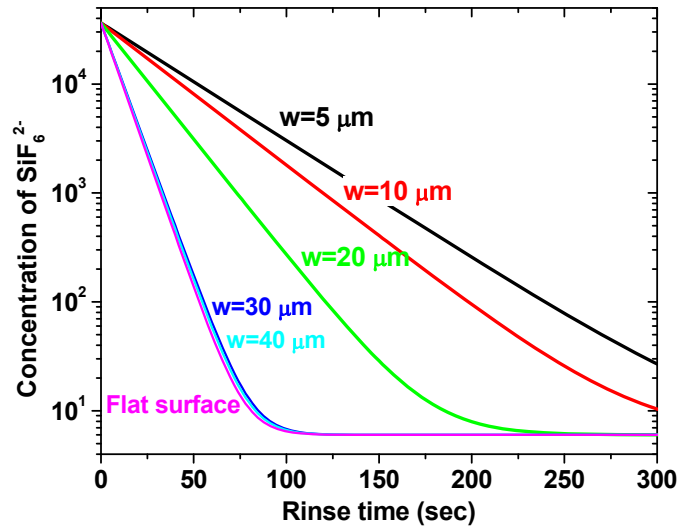
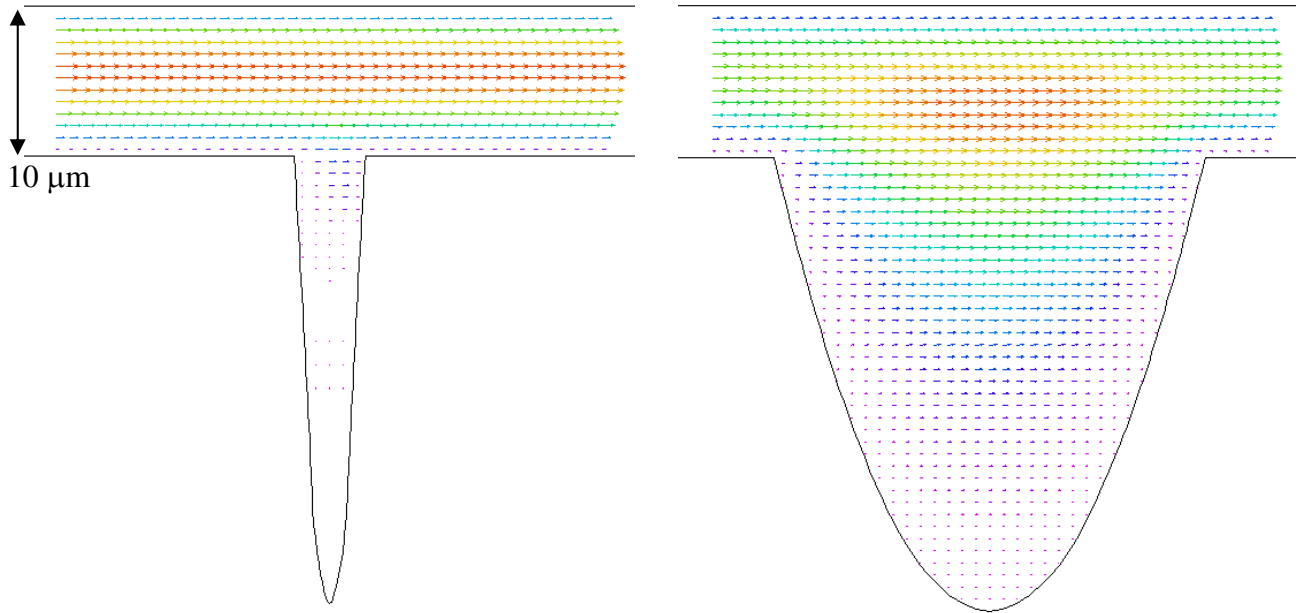


Figure 17: Optical micrographs of Samples H1-H4 illustrating the changes in morphology of the scratch with increase in etched amount.



(a)



(b)

Figure 18: (a) Calculated SiF_6^{2-} concentration at the center of an etched $30\text{ }\mu\text{m}$ deep trailing indent crack as a function of submersed rinse time for various width cracks (i.e. amount etched) using advection and diffusion transport in the boundary layer ($b=10\text{ }\mu\text{m}$, $v=0.0015\text{ m/s}$). (b) Calculated SiF_6^{2-} vector flux in a $5\text{ }\mu\text{m}$ wide (left side) and $30\text{ }\mu\text{m}$ wide (right side) scratch for the cases described in (a).